Energy & Environmental Science

PAPER

View Article Online
View Journal

Cite this: DOI: 10.1039/c5ee01179e

Abnormal crystal growth in $CH_3NH_3PbI_{3-x}Cl_x$ using a multi-cycle solution coating process†

Qingfeng Dong, Yongbo Yuan, Yuchuan Shao, Yanjun Fang, Qi Wang and Jinsong Huang*

Received 15th April 2015,
Accepted 23rd June 2015

DOI: 10.1039/c5ee01179e

www.rsc.org/ees

Recently, the efficiency of organolead trihalide perovskite solar cells has improved greatly because of improved material qualities with longer carrier diffusion lengths. Mixing chlorine in the precursor for mixed halide films has been reported to dramatically enhance the diffusion lengths of mixed halide perovskite films, mainly as a result of a much longer carrier recombination lifetime. Here we report that adding Cl containing precursor for mixed halide perovskite formation can induce the abnormal grain growth behavior that yields well-oriented grains accompanied by the appearance of some very large size grains. The abnormal grain growth becomes prominent only after multi-cycle coating of MAI : MACl blend precursor. The large grain size is found mainly to contribute to a longer carrier charge recombination lifetime, and thus increases the device efficiency to 18.9%, but without significantly impacting the carrier transport property. The strong correlation identified between material process and morphology provides guidelines for future material optimization and device efficiency enhancement.

Broader context

We report that the incorporation of Cl in precursor in the form of MAI : MACl for mixed halide perovskite formation by a multi-cycle coating interdiffusion method can induce abnormal grain growth behavior, forming large size perovskite grains. The large grain size is found to contribute mainly to a longer carrier recombination lifetime, but without significantly impacting the carrier transport property. The device power conversion efficiency was increased to 18.9%, and the devices showed no photocurrent hysteresis. Using the multi-cycle interdiffusion method, a strong correlation was observed between the abnormal grain growth, grain lateral size/thickness ratio enhancement and carrier lifetime/diffusion length increase. The multi-cycle interdiffusion process is a new method to fabricate mixed halide perovskite films different from the single-step method reported previously in its different capability in controlling morphology and microstructures. The study presented here pointed out a new direction to produce very large size grains by abnormal grain growth mechanism, which is crucial to achieve high efficiency polycrystalline thin film solar cells because reduced grain boundary area can effectively suppress charge recombination.

Organolead trihalide perovskites (OTPs) are emerging as a new generation of solution processable photovoltaic materials which are low-cost and nature-abundant.[1–16] OTPs have shown intriguing optoelectronic properties for photovoltaic applications, such as strong absorption in the ultraviolet-visible range, excellent crystallinity, bipolar carrier transport capability, and large charge diffusion length allowing for use in high performance perovskite photovoltaic devices (PPVs).[3,10,17,18] Methylammonium (MA) mixed lead halides, $CH_3NH_3PbX_{3-x}Y_x$ (X, Y = I, Br, Cl) have attracted most attention because of the high power conversion efficiency (PCE) of above 15% first achieved in PPVs with planar heterojunction (PHJ) structure.[1–16,19] It was later found that the diffusion length in mixed trihalide perovskite films, in the order of 1 micrometer, is ten times longer than that in triiodide perovskite films (~100 nm),[4] which is significant because a longer carrier diffusion length enables application of thicker mixed trihalide perovskite films for stronger absorption. The ultra-long carrier diffusion length in mixed halide OTPs was mainly caused by the much longer charge recombination lifetime.[4,20,21] However, the origin of the much longer diffusion length in mixed halide OTPs remains unclear in terms of material microscopic structure.

Here we report mixed halide perovskite films formed by a multi-cycle coating containing some very large mixed halide OTP grains with preferred orientation resulting from a new grain growth mode (abnormal growth). A correlation was identified between the film microstructure and electronic property and device performance. A ratio of high grain size to thickness dramatically reduced grain boundary (GB) area and the associated charge recombination, which contributed to improved device efficiency of up to 18.9%.

Department of Mechanical and Materials Engineering and Nebraska Center for Materials and Nanoscience, University of Nebraska-Lincoln, Lincoln, Nebraska 68588-0656, USA. E-mail: jhuang2@unl.edu

† Electronic supplementary information (ESI) available. See DOI: 10.1039/c5ee01179e

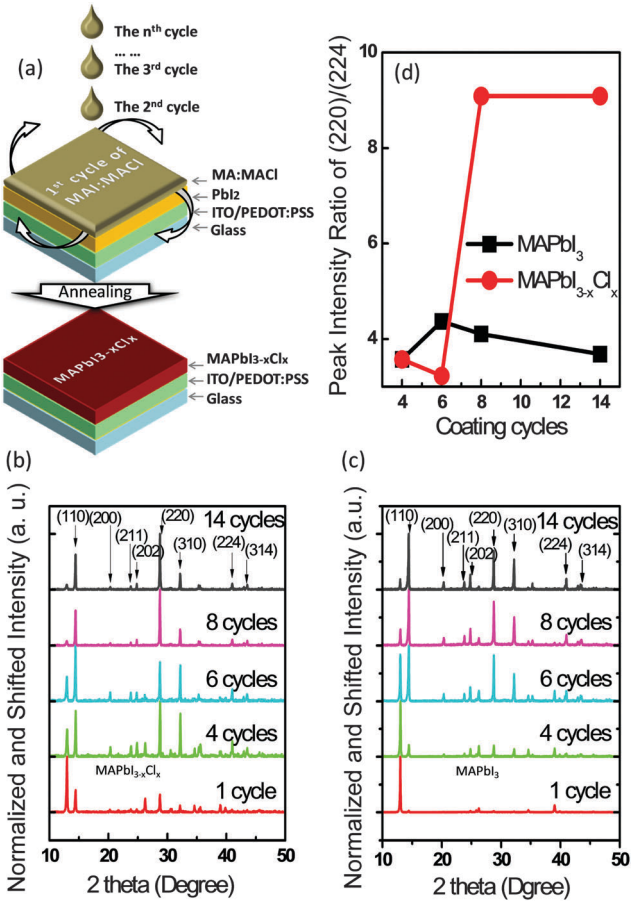

Fig. 1 (a) Schematics of formation of $MAPbClyI_{3-y}$ perovskite layer from multiple stacking layers of PbI_2 and MAI : MACl. (b and c) The XRD patterns of the $MAPbI_{3-x}Cl_x$ and $MAPbI_3$ films annealed at 110 °C for 90 min with different coating-cycles of MAI : MACl or MAI. (d) Intensity ratio of (220)/(224) peaks in the annealed $MAPbI_3$ and $MAPbI_{3-x}Cl_x$ films with different coating-cycles of MAI or MAI : MACl.

Cl was introduced from a mixed MAI : MACl precursor which has much higher solubility than $PbCl_2$ in common solvents such as 2-propanol. Fig. 1a illustrates the multi-cycle solution deposition and thermal annealing-induced interdiffusion processes of the PbI_2/MAI : MACl films. A PbI_2 layer formed the first coat, then MAI : MACl dissolved in an orthogonal solvent of 2-propanol was coated onto the PbI_2, followed by a thermal annealing-induced interdiffusion process to form homogeneous, pin-hole free perovskite films.[22] Here, the multi-cycle coating process was used for the first time for MAI : MACl precursor, and was found to allow precise control of the amount of Cl incorporated into the mixed halide OTPs. For each coating-cycle, a drop of MAI : MACl precursor solution was dripped onto the center of the spinning substrate, with the drop spreading immediately. After the previous layer had dried, another coating-cycle was initiated. The multi-cycle coating process allowed systematic control of the film thickness and mole ratio of the MAI : MACl and PbI_2 to form the stoichiometric mixed halide perovskite for optimized device efficiency.

Fig. 1b shows the wide spectral XRD patterns of annealed $MAPbI_{3-x}Cl_x$ films with different MAI : MACl coating-cycles. The crystal structure of the mixed halide perovskites still followed that of the $MAPbI_3$. One striking change of these diffraction patterns was that the intensity of the (220) peak at 28.7° increased significantly with more MAI : MACl coating-cycles, while the (310), (224), and (314) peaks at 32.0°, 41.0°, and 43.5° changed only a little. This indicates that the crystal grains in the mixed halide perovskite films formed by this new method had oriented grains. To identify the origin of grain orientation change, a set of control samples were fabricated using MAI for the multi-cycle coating. The XRD patterns of $MAPbI_3$ fabricated by multi-cycle coating are shown in Fig. 1c. The ratio of peak intensity of (220) to (224) planes is summarized in Fig. 1d for these two types of films with and without Cl after different coating-cycles. There was a dramatic increase in the ratio of (220)/(224) peak intensity in $MAPbI_{3-x}Cl_x$ films, but almost no change in $MAPbI_3$ films, providing solid evidence that the grain orientation change is caused by the Cl added in the precursor.

The grain growth process was studied by scanning electron microscopy (SEM) of the films formed by 280 nm PbI_2 reacting with different coating-cycles of MAI : MACl, and it was found that the preferred grain orientation originated from the abnormal grain growth behavior. SEM images of the perovskite films with 1, 4, 8, and 14 coating-cycles of MAI and MAI : MACl are shown in Fig. 2a–d, and the statistics of grain size derived from their SEM images (Fig. S1, ESI†) are shown in Fig. 2e and f. The grain size in the $MAPbI_{3-x}Cl_x$ films was significantly enlarged, and some very large grains appeared in the perovskite films with increased MAI : MACl coating-cycles. The grain size distribution histogram showed a transition from unimodal distribution to bimodal distribution for the $MAPbI_{3-x}Cl_x$ films. The grain size distribution histogram had only one peak in the films with single cycle MAI : MACl coating. However, the peak became broader and unsymmetrical with increased MAI : MACl coating-cycles; meanwhile, a new peak appeared corresponding to the very large grains, as labeled in Fig. 2e. The size variation of the grains in these two peaks as well as the largest grains is summarized in Fig. 2e with respect to the MAI : MACl coating-cycles. With increased MAI : MACl coating-cycles from 1 to 14, the average grain size increased 5.7 times from 228 nm to 1210 nm, and the largest grain size increased from 500 nm to 3.3 micrometers. Variations in thickness of the films with respect to the MAI : MACl coating-cycles are given in Fig. 2f, showing a quick increase in the first four coating-cycles and a slow saturation to 580 nm afterwards with depletion of PbI_2. The average grain sizes are thus significantly larger than the film thicknesses after several coating-cycles, with the largest grain size being six times that of the corresponding film thickness. This much larger grain size than film thickness, together with the appearance of elongated grains, are characteristic features of an abnormal grain growth process in the mixed halide perovskite films.[23–25]

To identify the driving force of the abnormal grain growth behavior, we examined the two possible origins, multi-cycle coating and Cl added in the precursor, by studying grain growth behavior in $MAPbI_3$ control samples fabricated in the same way as the $MAPbI_{3-x}Cl_x$ samples. As shown in the SEM images in Fig. 2g–j, the multi-cycle coating process only slightly increased

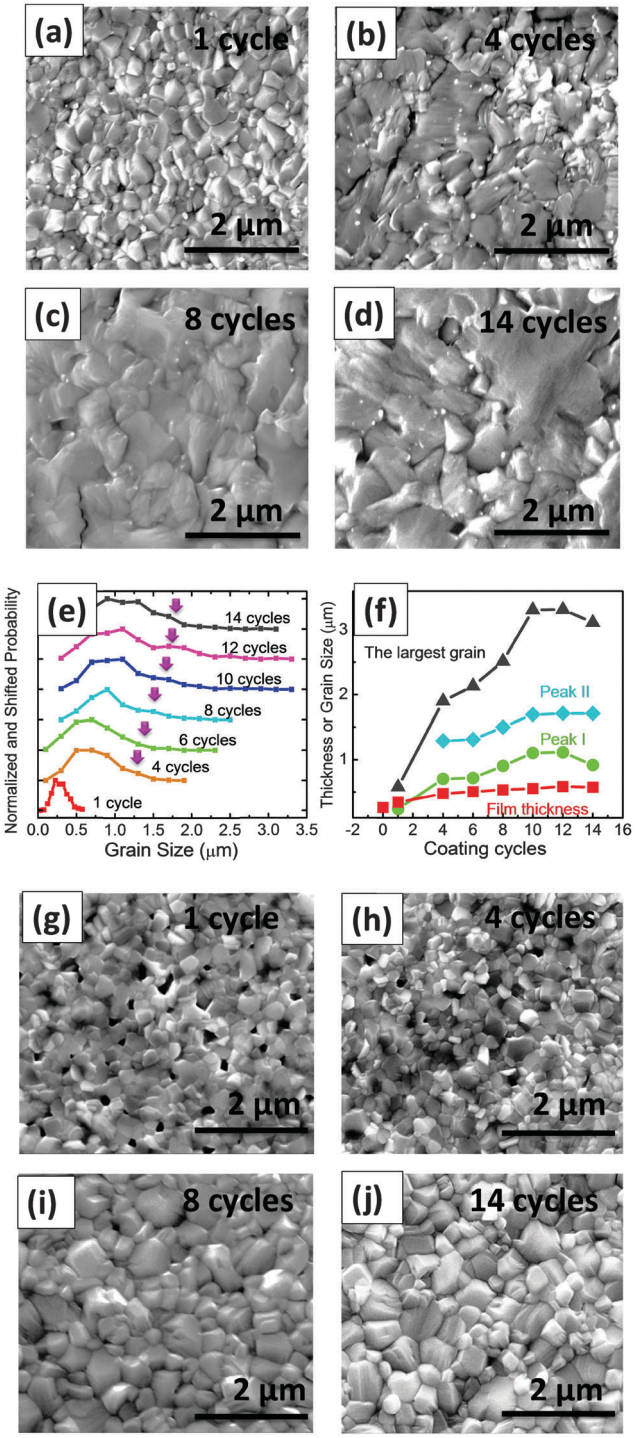

Fig. 2 (a–d) SEM images of the perovskite films with varied layers of MAI : MACl. (e) Statistics of grain sizes in 17 μm × 17 μm E images of the perovskite films with varied coating-cycles of MAI : MACl. (f) Film thickness and grain size with respect to the different coating-cycles of MAI : MACl. (g–j) SEM images of the perovskite films with varied coating-cycles of MAI.

the grain size of $MAPbI_3$ from 174 nm to 273 nm with increasing coating-cycles from 1 to 8. This can be explained by the multi-cycle coating process providing a longer duration in the solvent environment to promote longer range diffusion of precursor ions, as demonstrated by the solvent annealing method used. In contrast, there were no very large grains in $MAPbI_3$ films, indicating that the Cl added in the precursor was the main originator of the abnormal grain growth behavior.

We come to the scenario that enlarged grain by Cl incorporation correlates with the different crystallographic orientations in $MAPbI_{3-x}Cl_x$ compared with $MAPbI_3$. In a thin film growth process, the growth rate of a grain is determined by the Gibbs free energy of the precursor and formed perovskite, which includes not only chemical energy difference, but also the surface energy and interface energy (and therefore crystallographic orientation) of the grains.[23–25] Grains with some special crystallographic orientations can have smaller surface energy and are easier to grow.[23–25] As $MAPbI_3$ is tetragonal, with less symmetry than cubic structures, there can be large differences in the surface energy between different crystal planes/facets. We speculated that the (220) plane has the smallest surface energy or interfacial energy because more grains have this orientation to minimize the total free energy of the system. With increasing coating-cycles, the (220) oriented grains grew faster by consuming neighboring non-oriented grains, either by regular grain growth or grain attachment process. This resulted in the grain distribution shifting to large grain size, as evidenced by the observed bimodal distribution as well as the significantly increased ratio between the XRD intensity of (220) peaks and that of the (310), (224), and (314) peaks with increased coating-cycles.[23–27] The added Cl in the precursor promotes secondary grain growth by slowing the crystal formation process. It has been reported that Cl in the precursor causes formation of intermediate phases,[28] also observed by us in this study,[29] which reduces crystallization of $MAPbI_3$. Quick formation of $MAPbI_3$ is expected to form randomly oriented grains because of the randomness in the nucleation process, whereas slowed crystallization allows the nucleus to adjust the orientation to minimize the total Gibbs free energy. Our recent study using additional solvent vapor treatment during the film nucleation process confirmed this scenario.[30] The multi-cycle coating process should contribute to the grain growth process rather than the grain nucleation process for formation of larger grains, because most of the grains are formed in the first few cycles of coating.

It should be emphasized that this is the first time that a secondary grain growth process has been identified in mixed halide perovskite films. The average and largest grain sizes are ~1.1 and ~3.3 μm, respectively, which are twofold and sixfold that of the corresponding film thicknesses. The ratio of large grain size to film thickness was important for their application in polycrystalline thin film photovoltaic devices, because a decreased grain boundary area contributes decreased charge recombination. As the average grain size is significantly larger than the film thickness, most of the charge carrier can efficiently transport across the perovskite films in a single crystal grain and be collected without the need to cross any grain boundary.[22]

The influence of Cl incorporation and multi-cycle coating was investigated on photovoltaic device performance. All the photovoltaic devices have a structure of indium tin oxide (ITO)/poly(3,4-ethylenedioxythiophene) poly(styrenesulfonate) (PEDOT:PSS)/$MAPbI_3$ or $MAPbI_{3-x}Cl_x$/[6,6]-phenyl-C_61-butyric acid methyl ester

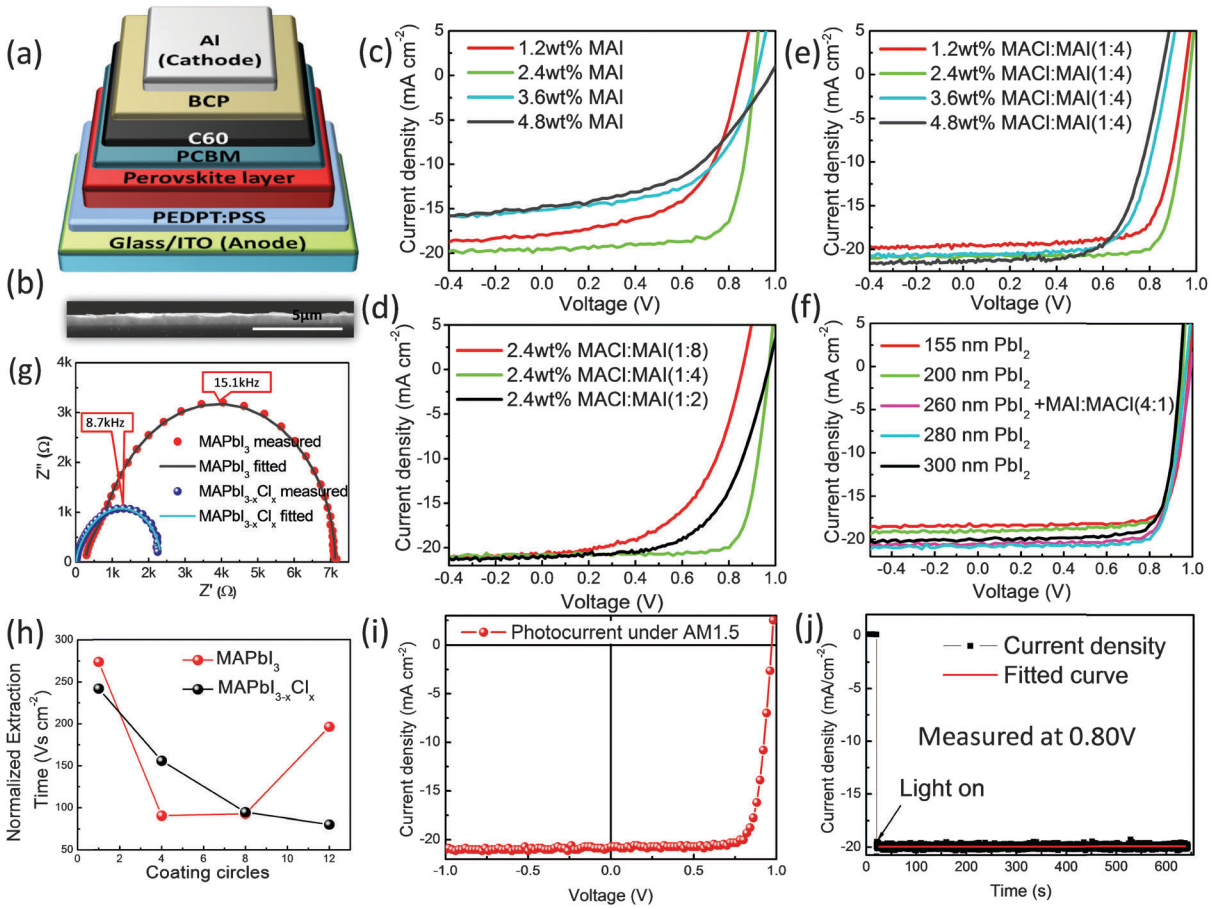

Fig. 3 (a) Device structure of perovskite solar cells. (b) SEM image of the cross-section of a $MAPbI_{3-x}Cl_x$ perovskite film. (c–f) *J–V* curves for optimized multi-cycle coating interdiffusion processed perovskite solar cells based on (c) PbI_2 and MAI precursor with different concentrations; (d) PbI_2 and MACl:MAI precursor with different concentrations and (e) different MACl : MAI ratio; (f) MACl : MAI (2.4 wt%, mol : mol 1 : 4) and PbI_2 layer with different thickness. (g) Nyquist plot of impedance spectra of $MAPbI_3$ (red dot) and $MAPbI_{3-x}Cl_x$ (blue dot) devices, respectively. Dots are measured results and lines are fitted curves. (h) Charge extraction time of optimized $MAPbI_3$ and $MAPbI_{3-x}Cl_x$ perovskite photovoltaic devices with varied coating-cycles. (i) *J–V* curve of the optimized $MAPbI_{3-x}Cl_x$ perovskite photovoltaic devices on PEDOT:PSS and (j) steady-state photocurrent output at the maximum power point (0.80 V).

(PCBM 10 nm)/C60 (20 nm)/2,9-dimethyl-4,7-diphenyl-1,10-phenanthroline (BCP, 7.5 nm)/aluminum (Al, 100 nm) as shown in Fig. 3a.[11,31] Device fabrication and measurement details are given in the experiment section. As shown by the cross-section SEM in Fig. 3b, all showed continuous, compact, pin-hole free perovskite films formed on PEDOT:PSS, allowing fabrication of high performance devices at high yield. As the performance of the photovoltaic devices can be changed by multiple factors including the Cl ratio in MAI : MACl precursor, organic and inorganic precursor ratio, and the perovskite film thickness, systematic optimization was performed by varying these parameters one by one. Here, the influence of Cl incorporation on device performance was investigated by comparing $MAPbI_{3-x}Cl_x$ PPVs and $MAPbI_3$-based control devices with all conditions kept the same except use of organic precursors with PEDOT:PSS as the hole transport layer (HTL). We first optimized devices by varying the MAI or MAI : MACl concentration for an appropriate amount of MAI or MAI : MACl increase between two cycles for the best device performance. As shown in Fig. 3c and d, the $MAPbI_3$ and $MAPbI_{3-x}Cl_x$ devices showed the best performance with 2.4 wt% organic precursor solution. At this concentration, MAI : MACl ratio varying from 8 : 1 to 2 : 1 was used in precursor and the best $MAPbI_{3-x}Cl_x$ devices achieved with MAI : MACl ratio of 4 : 1. The best device performance was achieved after optimizing the active layer thickness by changing the starting PbI_2 layer thickness. The best coating-cycles were optimized for each parameter as shown in Fig. S2–S4 (ESI†). The photocurrent *J–V* curves of the optimized PPVs based on $MAPbI_3$ as well as $MAPbI_{3-x}Cl_x$ are shown in Fig. 3c–f. Optimized PCEs were obtained with seven coating-cycles for the $MAPbI_3$ PPVs and eight to ten cycles for the $MAPbI_{3-x}Cl_x$ PPVs with 2.4 wt% MAI : MACl (4 : 1 mol : mol) precursor. The optimized $MAPbI_3$ PPVs had a J_{SC} of 19.61 mA cm^{-2}, a V_{OC} of 0.91 V, a fill factor (FF) of 75.14%, and a PCE of 13.41%, and the optimized $MAPbI_{3-x}Cl_x$ PPVs had a J_{SC} of 20.71 mA cm^{-2}, a V_{OC} of 0.97 V, a FF of 79.69%, and a PCE of 16.01%. There was a 5–10% increase in V_{OC}, FF, and J_{SC} in the $MAPbI_{3-x}Cl_x$ PPVs compared with $MAPbI_3$ PPVs, resulting in a ~20% higher PCE as a result of Cl addition to the precursor.

To understand the origin of the enhanced performance for devices based on $MAPbI_{3-x}Cl_x$ rather than $MAPbI_3$, the charge carrier lifetime and motility were measured, and corresponding charge diffusion lengths were calculated. Previously the free charge lifetime was mainly determined by spontaneous radiative charge recombination lifetime, which gives only the lower limit of charge recombination lifetime.[4] Here the charge carrier recombination lifetime under real device working conditions was determined by impedance spectroscopy measurement as the product of the chemical capacitance and recombination resistance.[32] Fig. 3g shows the Nyquist plot of the measured and fitted impedance spectra of the $MAPbI_3$ and $MAPbI_{3-x}Cl_x$ devices with PEDOT:PSS HTL, respectively. The equivalent circuit used to fit the measured impedance spectra is shown in Fig. S6 (ESI†). The charge carrier lifetime under short circuit conditions is 18.3 μs for $MAPbI_{3-x}Cl_x$ devices, longer than the 10.5 μs for the $MAPbI_3$ devices; however, the difference in carrier recombination lifetime induced by Cl incorporation is much less than reported previously. The longer recombination lifetime indicates a decrease in charge recombination, which confirms our scenario that the large ratio of grain size to the thickness for the thin film is beneficial in reducing charge recombination. The reduced charge recombination explains the higher V_{OC}, FF and J_{SC} in the $MAPbI_{3-x}Cl_x$ devices. The charge extraction time (τ) of $MAPbI_{3-x}Cl_x$ and $MAPbI_3$ devices was derived by fitting the transient photocurrent decay curve with single exponential decay function, and was normalized by the film thickness and built-in potential, as shown in Fig. 3h. It is noted that the measured τ is determined by the mobilities of both the perovskite layer and the charge transport layers such as fullerene and BCP. Nevertheless, the τ variation here should reflect the transport property change of the perovskite layers, because the electron transport layers were the same for the $MAPbI_3$ and $MAPbI_{3-x}Cl_x$ devices. The τ of $MAPbI_3$ films decreased initially with coating-cycles, and then increased after eight coating-cycles. In contrast, the τ kept increasing in $MAPbI_{3-x}Cl_x$ films with increased coating-cycles, indicating increasing carrier mobility. The lower carrier mobility in both types of perovskite films with less than eight coating-cycles could be caused by residual PbI_2, which retards the charge collection from the perovskite layers. The $MAPbI_{3-x}Cl_x$ and $MAPbI_3$ films, which led to the optimized device efficiency, have comparable carrier mobility. This indicates that transport property was not improved by Cl incorporation despite the better alignment of the grain orientation. It suggests that the function of Cl incorporation mainly caused microstructure change of perovskite film with formation of larger grain, which reduces charge recombination.

Photocurrent hysteresis occurs in many perovskite PPVs, which is a serious hindrance for PPV development and accurate characterization of device efficiencies. To find out whether there was photocurrent hysteresis[33] in our devices, we measured the transient response of the devices, and scanned the photocurrents with increasing or decreasing voltage. As shown in Fig. S5a (ESI†), the photocurrents rose quickly to maximum in sub-millisecond, limited by the spin-rate of our chopper. This was verified using the same response curve by replacing the PPV devices with a silicon diode (Hamamatsu S1133). The fast photoresponse of PPVs indicates that there was a low trap density in the optimized perovskite films or at the interfaces of the devices. As shown in Fig. S5b (ESI†), no obvious photocurrent hysteresis was observed in our optimized devices by changing the photocurrent sweep rates from 0.15 V s^{-1} to 0.3 V s^{-1} or the sweep directions. The stabilized efficiency is the same as that measured from the *J–V* curve (Fig. 3i and j). Another merit of the multi-cycle coating method to fabricate mixed halide PPVs is that it is easy to reproduce the optimized devices because of the precise control of the optimized ratio of MAI : MACl to PbI_2, providing an excellent yield of high PCE devices. The statistics of the FF, V_{OC}, J_{SC}, and PCE based on 30 mixed halide PPVs with PEDOT:PSS as HTL from five batches are shown in Fig. S5c–f (ESI†), with a high average FF of 79% and highest PCE of 16.01% for the device fabricated on PEDOT:PSS.

Finally, poly[bis(4-phenyl)(2,4,6-trimethylphenyl)amine] (PTAA) was recently shown to be a better HTL than PEDOT:PSS because of its larger work function and non-wetting surface.[34–36] We replaced PEDOT:PSS by PTAA, and conducted the same device optimization. The *J–V* curves as well as their external quantum efficiency (EQE) spectra of optimized devices based on PTAA are shown in Fig. 4. The device with PTAA has a much larger V_{OC} to 1.1 V and slightly improved J_{SC} to 21.96 mA cm^{-2}, resulting in a highest device efficiency of 18.9%. Similarly these devices show very small photocurrent hysteresis when the current scanning direction and rate are reversed. The large J_{SC} is consistent with the integrated photocurrent of 21.24 mA cm^{-2} from the EQE (Fig. 4b).

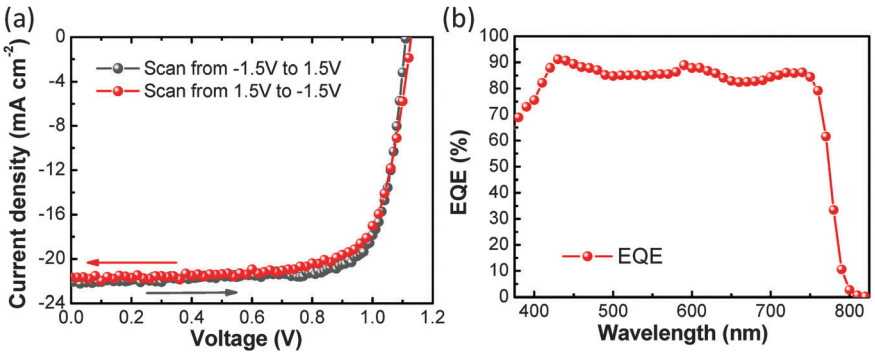

Fig. 4 (a) *J–V* curves for optimized multi-cycle coating interdiffusion processed $MAPbI_{3-x}Cl_x$ perovskite solar cells on PTAA and (b) the EQE spectra.

In conclusion, we have presented a comprehensive study on the mechanism of enhanced carrier diffusion length in mixed halide perovskite by revealing the correlation of fabrication process, material grain growth, composition, microstructure, and electronic properties. Using a multi-cycle interdiffusion method, a strong correlation was observed between the abnormal grain growth, grain lateral size/thickness ratio enhancement, and carrier lifetime/diffusion length increase. The multi-cycle interdiffusion method to fabricate mixed halide perovskite films is completely different from the single step method reported previously in its capability to control morphology and microstructures. The study presented here points to a new direction to produce very large size grains by an abnormal grain growth mechanism, which is crucial for achieving high efficiency polycrystalline thin film solar cells because reduced grain boundary area can effectively reduce charge recombination. The film fabrication should not be limited to a solution process because continuous evaporation of Cl containing precursor is also feasible by vapor deposition.

Methods

PbI_2 and MAI : MACl precursor preparation

MAI was synthesized using the method described by Michael M. Lee, *et al.*[5] MACl was synthesized by the reaction of methylamine (13.5 mL, 40% w/w aq. soln., Alfa Aesar) with a concentrated aqueous solution of hydrochloric acid (23.5 mL, 36.5 wt% in water, Alfa Aesar) at 0 °C for 2 h with constant stirring under a nitrogen atmosphere, followed by a crystallized purification and dry process, which was the same as for the preparation of MAI. MAI : MACl precursor was prepared by mixing MAI and MACl in 2-propanol for different blend ratio and concentration. PbI_2 precursor was prepared by dissolving PbI_2 in DMF.

Film and photovoltaic device fabrication

For perovskite film fabrication, all solutions were stirred at 100 °C to become fully dissolved before use. First, the PbI_2 hot solution was spun onto a PEDOT:PSS or PTAA coated ITO glass substrate. Then, after the previous layer had dried, MAI or MAI : MACl solution was dripped onto the previous layers during spinning of substrate for multi-cycle coating. The substrate continued spinning during the multi-cycle, with each layer drying after spinning for 3 seconds after the solution spread of each cycle. In this work, 10 μL of 2.4 wt% MAI or MAI : MACl (4 : 1 mol : mol) solution was dripped onto the PbI_2 film at 6000 rpm, followed by dripping of another 10 μL of MAI or MAI : MACl (4 : 1 mol : mol) onto the layers every 3 seconds during continuous spinning of substrate. After the coating of MAI or MAI : MACl, the film was transferred onto a 60 °C hotplate. For perovskite films with PEDOT:PSS HTL, 20 μL DMF was added to the petri dish of samples before the annealing process, which constituted 90 minutes of solvent-assisted thermal annealing at 110 °C. For perovskite films with PTAA HTL, a lower annealing temperature of 60 °C was used. For photovoltaic devices, 2 wt% solution of PCBM in DCB was spun on the annealed perovskite film, followed by an additional 60 min of annealing. Then the device was completed by sequence depositing 20 nm C60, 7.5 nm BCP, and 100 nm Al. The device *J–V* curve measurement was conducted in a nitrogen filled glove-box.

Film and device characterization

XRD measurements were performed with a Rigaku D/Max-B X-ray diffractometer with Bragg–Brentano parafocusing geometry, a diffracted beam monochromator, and a conventional copper target X-ray tube set to 40 kV and 30 mA. The single path absorption was measured using an Evolution 201 UV-Visible spectrometer (Thermo Scientific). A Quanta 200 FEG Environmental Scanning Electron Microscope (ESEM) using a field-emission gun (FEG) electron source was used to scan the film morphology. The films were first covered with a thin layer of gold coated using a Cressington 108 Auto Sputter Coater before the SEM measurement. The photocurrent curves were measured under simulated AM 1.5G irradiation (100 mW cm^{-2}) using a Xenon-lamp-based solar simulator (Oriel 67005, 150 W Solar Simulator). A Schott visible-color glass-filtered (KG5 color-filtered) Si diode (Hamamatsu S1133) was used to calibrate the light intensity before photocurrent measurement to avoid optical mismatch. Impedance spectroscopy was recorded under AM 1.5G illumination by the E4980A Precision LCR Meter at frequencies from 0.2 to 2000 kHz from Agilent with homemade software. The device area was 9 mm^2.

Acknowledgements

We are grateful for financial support from the Department of Energy under the Award DE-EE0006709 and the National Science Foundation under the Award ECCS-1252623.

References

1 A. Kojima, K. Teshima, Y. Shirai and T. Miyasaka, *J. Am. Chem. Soc.*, 2009, **131**, 6050.
2 J. M. Ball, M. M. Lee, A. Hey and H. J. Snaith, *Energy Environ. Sci.*, 2013, **6**, 1739.
3 G. Xing, N. Mathews, S. Sun, S. S. Lim, Y. M. Lam, M. Grätzel, S. Mhaisalkar and T. C. Sum, *Science*, 2013, **342**, 344.
4 S. D. Stranks, G. E. Eperon, G. Grancini, C. Menelaou, M. J. Alcocer, T. Leijtens, L. M. Herz, A. Petrozza and H. J. Snaith, *Science*, 2013, **342**, 341.
5 M. M. Lee, J. Teuscher, T. Miyasaka, T. N. Murakami and H. J. Snaith, *Science*, 2012, **338**, 643.
6 A. K. Rath, M. Bernechea, L. Martinez, F. P. G. de Arquer, J. Osmond and G. Konstantatos, *Nat. Photonics*, 2012, **6**, 529.
7 A. Marchioro, J. Teuscher, D. Friedrich, M. Kunst, R. Van De Krol, T. Moehl, M. Grätzel and J.-E. Moser, *Nat. Photonics*, 2014, **8**, 250.
8 O. Malinkiewicz, A. Yella, Y. H. Lee, G. M. Espallargas, M. Graetzel, M. K. Nazeeruddin and H. J. Bolink, *Nat. Photonics*, 2014, **8**, 128.
9 D. Liu and T. L. Kelly, *Nat. Photonics*, 2013, **8**, 133.

10 J. H. Heo, S. H. Im, J. H. Noh, T. N. Mandal, C.-S. Lim, J. A. Chang, Y. H. Lee, H.-j. Kim, A. Sarkar and M. K. Nazeeruddin, *Nat. Photonics*, 2013, **7**, 486.
11 T. Leijtens, G. E. Eperon, S. Pathak, A. Abate, M. M. Lee and H. J. Snaith, *Nat. Commun.*, 2013, **4**, 2885.
12 H.-S. Kim, I. Mora-Sero, V. Gonzalez-Pedro, F. Fabregat-Santiago, E. J. Juarez-Perez, N.-G. Park and J. Bisquert, *Nat. Commun.*, 2013, **4**, 2242.
13 M. Liu, M. B. Johnston and H. J. Snaith, *Nature*, 2013, **501**, 395.
14 I. Chung, B. Lee, J. He, R. P. Chang and M. G. Kanatzidis, *Nature*, 2012, **485**, 486.
15 J. Burschka, N. Pellet, S.-J. Moon, R. Humphry-Baker, P. Gao, M. K. Nazeeruddin and M. Grätzel, *Nature*, 2013, **499**, 316.
16 Q. Chen, H. Zhou, Z. Hong, S. Luo, H.-S. Duan, H.-H. Wang, Y. Liu, G. Li and Y. Yang, *J. Am. Chem. Soc.*, 2013, **136**, 622.
17 G. Hodes, *Science*, 2013, **342**, 317.
18 P. Docampo, J. M. Ball, M. Darwich, G. E. Eperon and H. J. Snaith, *Nat. Commun.*, 2013, **4**, 2761.
19 B. V. Lotsch, *Angew. Chem., Int. Ed.*, 2014, **53**, 635.
20 E. Edri, S. Kirmayer, A. Henning, S. Mukhopadhyay, K. Gartsman, Y. Rosenwaks, G. Hodes and D. Cahen, *Nano Lett.*, 2014, **14**, 1000.
21 S. Colella, E. Mosconi, P. Fedeli, A. Listorti, F. Gazza, F. Orlandi, P. Ferro, T. Besagni, A. Rizzo and G. Calestani, *Chem. Mater.*, 2013, **25**, 4613.
22 Z. Xiao, C. Bi, Y. Shao, Q. Dong, Q. Wang, Y. Yuan, C. Wang, Y. Gao and J. Huang, *Energy Environ. Sci.*, 2014, **7**, 2619.
23 C. V. Thompson and R. Carel, *J. Mech. Phys. Solids*, 1996, **44**, 657.
24 C. V. Thompson, *Annu. Rev. Mater. Sci.*, 2000, **30**, 159.
25 C. V. Thompson, *Annu. Rev. Mater. Sci.*, 1990, **20**, 245.
26 P. W. Liang, C. C. Chueh, X. K. Xin, F. Zuo, S. T. Williams, C. Y. Liao and A. K. Y. Jen, *Adv. Energy Mater.*, 2015, **5**, 1400960.
27 J. Qiu, Y. Qiu, K. Yan, M. Zhong, C. Mu, H. Yan and S. Yang, *Nanoscale*, 2013, **5**, 3245.
28 W. Zhang, M. Saliba, D. T. Moore, S. K. Pathak, M. T. Hörantner, T. Stergiopoulos, S. D. Stranks, G. E. Eperon, J. A. Alexander-Webber and A. Abate, *Nat. Commun.*, 2015, **6**, 6142.
29 J. Chae, Q. Dong, J. Huang and C. Andrea, unpublished.
30 J. Lian, Q. Wang, Y. Yuan, Y. Shao and J. Huang, *J. Mater. Chem. A*, 2015, **3**, 9146.
31 Q. Wang, Y. Shao, Q. Dong, Z. Xiao, Y. Yuan and J. Huang, *Energy Environ. Sci.*, 2014, **7**, 2359.
32 J. Bisquert, F. Fabregat-Santiago, I. n. Mora-Seró, G. Garcia-Belmonte and S. Giménez, *J. Phys. Chem. C*, 2009, **113**, 17278.
33 H. J. Snaith, A. Abate, J. M. Ball, G. E. Eperon, T. Leijtens, N. K. Noel, S. D. Stranks, J. T.-W. Wang, K. Wojciechowski and W. Zhang, *J. Phys. Chem. Lett.*, 2014, **5**, 1511.
34 Y. Deng, E. Peng, Y. Shao, Z. Xiao, Q. Dong and J. Huang, *Energy Environ. Sci.*, 2015, **8**, 1544.
35 C. Bi, Q. Wang, Y. Shao, Y. Yuan, Z. Xiao and J. Huang, *Nat. Commun.*, DOI: 10.1038/ncomms8747.
36 Q. Wang, C. Bi and J. Huang, *Nano Energy*, 2015, **15**, 275–280.